RESEARCH ARTICLE

ADVANCED FUNCTIONAL MATERIALS
www.afm-journal.de

Stabilizing Cationic Palladium Single-Atom Sites on Heteroatom-Doped Carbon for Selective Hydrogen Peroxide Electrosynthesis

Guilherme V. Fortunato, Alexander Gunnarson, Hannaneh Hosseini, Xiangyu You, Pallabi Bhuyan, Ji Sik Choi, Hyo Sang Jeon, Xingshen Zhao, Julio C. Lourenço, Sumin Lim, Huize Wang, Ana Guilherme Buzanich, Martin Radtke, Paul Paciok, Marcos R.V. Lanza, Ferdi Schüth,* and Marc Ledendecker**

Single-atom catalysts (SACs) offer significant potential for the sustainable electrosynthesis of hydrogen peroxide (H_2O_2) via the two-electron oxygen reduction reaction ($2e^-$ ORR). However, their practical deployment is hindered by challenges related to limited operational stability and intricate synthetic procedures. Here, a family of cationic Pd single-atom complexes anchored on nitrogen-, sulfur-, and dual N,S-doped hollow carbon spheres (HCS) is reported, prepared via mild vapor-phase doping combined with wet impregnation of $Pd(acac)_2$. Systematic tuning of the heteroatom environment enables precise control over the Pd electronic state and local coordination, enhancing selectivity and long-term stability under acidic, peroxide-rich conditions. Operando ICP-MS and advanced spectroscopy reveal that sulfur-doping induces favorable charge redistribution, reinforcing Pd–support interactions and suppressing demetallation, while nitrogen doping enhances ORR activity. Notably, dual N,S-co-doping achieves a synergistic balance between catalytic performance and stability. This strategy offers a rational design framework for robust ligand-containing SACs, advancing sustainable electrocatalytic technologies well beyond H_2O_2 synthesis.

1. Introduction

Single-atom catalysts (SACs) have garnered significant attention due to their ability to maximize atomic efficiency, provide uniform active sites, and enable precise control over electronic properties for a wide range of catalytic transformations.[1–5] These attributes make SACs particularly attractive for electrocatalytic reactions, where a delicate balance between activity, selectivity, and stability is essential.

A promising strategy for preparing SACs involves immobilizing active organometallic complexes, such as bioinspired macrocycles[6–15] or metal salts,[16–18] onto high-surface-area carbon supports that offer abundant anchoring sites. Heteroatom doping, especially with nitrogen[19–28] and sulfur[21,26,29–34] has emerged as an effective approach to introduce electron-rich sites within carbon frameworks, modulate the

---

G. V. Fortunato, X. You, P. Bhuyan, J. S. Choi, X. Zhao, J. C. Lourenço, S. Lim, H. Wang, M. Ledendecker
Sustainable Energy Materials
TUM Campus Straubing for Biotechnology and Sustainability
Technical University of Munich
Schulgasse 22, 94315 Straubing, Germany
E-mail: g.fortunato@tum.de; marc.ledendecker@tum.de

A. Gunnarson, H. Hosseini, F. Schüth
Department of Heterogeneous Catalysis
Max-Planck-Institut für Kohlenforschung
Kaiser-Wilhelm-Platz 1, 45470 Mülheim an der Ruhr, Germany
E-mail: schueth@kofo.mpg.de

The ORCID identification number(s) for the author(s) of this article can be found under https://doi.org/10.1002/adfm.202516600

DOI: 10.1002/adfm.202516600

A. Gunnarson
Department of Physics
Technical University of Denmark
Kongens Lyngby 2800, Denmark

H. S. Jeon
Sustainable Energy Research Division
Korea Institute of Science and Technology
5, Hwarang-ro 14-gil, Seongbuk-gu, Seoul 02792, Republic of Korea

J. C. Lourenço, M. R. Lanza
Institute of Chemistry of São Carlos
University of São Paulo
Avenida Trabalhador São-Carlense 400, São Carlos, SP 13566-590, Brazil

H. Wang, M. Ledendecker
Helmholtz Institute Erlangen-Nürnberg for Renewable Energy (IET-02)
Forschungszentrum Jülich GmbH
Cauerstr. 1, 91058 Erlangen, Germany

A. G. Buzanich, M. Radtke
Bundesanstalt für Materialforschung und -prüfung (BAM)
Richard Willstaetter Str. 11, 12489 Berlin, Germany

P. Paciok
Ernst Ruska-Centre (ER-C-1)
Forschungszentrum Jülich GmbH
Leo-Brandt-Straße 1, 52428 Jülich, Germany

local coordination environment, and enhance metal–support interactions.[21–24,26,31,33–36] This method has been widely applied in thermocatalysis, offering well-defined cationic metal centers and tunable activity through ligand modification.[16–18,37,38] More recently, its translation to electrocatalysis has shown promise: Pd(acac)$_2$-impregnated carbon-based SACs have demonstrated high activity and selectivity over 90% for the two-electron oxygen reduction reaction (2e$^-$ ORR) toward hydrogen peroxide (H_2O_2).[17,39]

Despite these advantages, the practical deployment of SACs remains constrained by inherent challenges in maintaining structural and chemical stability under both synthesis and operational conditions. Thermodynamically, isolated metal atoms tend to migrate, aggregate, or leach, leading to a loss of atomic dispersion and a consequent decline in catalytic performance over time.[1,22,40–44] In particular, weak interactions between Pd(acac)$_2$ complexes and undoped carbon supports often lead to significant demetallation and active site loss under peroxide-rich acidic conditions.[17,39]

To address this knowledge gap, we conducted a systematic investigation into the electrochemical stability and catalytic performance of cationic Pd SACs anchored on nitrogen-, sulfur-, and dual N,S-doped hollow carbon spheres (HCS), aiming to elucidate the role of heteroatom identity in stabilizing isolated metal centers. Using a hard-templating synthesis strategy combined with molecular heterocyclic precursors, we prepared a series of structurally comparable, impurity-free carbon supports with precisely controlled heteroatom compositions. Operando inductively coupled plasma–mass spectrometry (ICP–MS) and ex situ spectroscopic techniques were used to monitor Pd dissolution and probe the local coordination environment. Complementary structural and electronic analyses were performed using high-resolution electron microscopy and X-ray absorption spectroscopy.

In addition to demonstrating high selectivity for the 2e$^-$ ORR, dual N,S-doped SACs exhibited exceptional resistance to demetallation, attributed to charge redistribution between the support and the metal center, which in turn strengthens Pd–support interactions. These findings provide critical insights into the cooperative effects of heteroatom doping in stabilizing ligand-containing SACs and offer a rational design strategy for developing robust single-atom electrocatalysts for sustainable chemical production.

2. Results and Discussion

2.1. Design Strategy and Material Synthesis

To achieve high Pd dispersion and stable anchoring, we developed N-, S- and N,S-doped hollow carbon spheres (HCS) via chemical vapor deposition (CVD) of pyrrole, thiophene, and thiazole—heteroatom-rich precursors selected for their high N, S and N,S content, suitable volatility, and clean decomposition at 750 °C (**Figure 1A**). This vapor-phase doping strategy enables efficient and uniform incorporation of nitrogen and/or sulfur across the carbon matrix, directly tuning the support's electronic structure and anchoring sites. TEM images (Figures 1B–D; Figure S1, Supporting Information) confirm the formation of well-defined hollow spheres with uniform shells. All materials exhibit mesoporous texture (Figure 1E and Table S1, Supporting Information), with comparable surface areas and minor differences in pore profiles. X-ray diffraction patterns (Figure S2, Supporting Information) reveal two broad diffraction features at ≈25° and ≈43°, corresponding to the (002) and (100) planes of graphitic carbon. The absence of sharp reflections confirms the largely amorphous nature of all HCS supports, as expected for soft-carbon materials synthesized in the absence of a graphitization catalyst.[45,46] Slight variations in the intensity and position of the (002) peak across the samples may reflect differences in local ordering or interlayer spacing induced by heteroatom doping.[47–49] Raman spectroscopy (Figure S2B, Supporting Information) further corroborates the impact of heteroatom doping on the carbon framework. All samples exhibit the characteristic D (≈1350 cm^{-1}) and G (≈1580 cm^{-1}) bands, corresponding to disordered and graphitic sp^2 carbon domains, respectively.[50] The intensity ratio (I_D/I_G) increases from 0.97 in N-HCS to 1.01 in S-HCS, and 0.99 in N,S-HCS, indicating a higher degree of structural disorder introduced by heteroatom incorporation. The larger increase observed for S-HCS suggests a stronger defect-inducing effect due to sulfur's larger atomic radius.[50,51] Thermogravimetric analysis results (c.f. Figure S2B, Supporting Information) indicate relatively similar carbon structures, with N-HCS and N,S-HCS having higher thermal stability, likely due to nitrogen incorporation.[51] X-ray photoelectron spectroscopy (XPS) analysis (c.f. Figure 1F,G; Figures S3–S5, Supporting Information) shows consistent doping levels (≈6–8 at.%) across all samples. Deconvolution of the N 1s spectra indicates pyrrolic and pyridinic species as the dominant nitrogen moieties, while the S 2p spectra reveal thiophenic sulfur in S-HCS and additional oxidized sulfur species (≈168 eV) in N,S-HCS. The latter are attributable either to oxidized sulfur or to sulfur in proximity to nitrogen, likely formed during HF leaching and stabilized by adjacent nitrogen atoms.[52,53]

Building upon a previously established method, Pd SACs were synthesized via wet impregnation (WI) onto the heteroatom-doped HCS (**Figure 2A**), using Pd(acac)$_2$ dissolved in anhydrous acetone.[16,17] This approach has been used for non-heteroatom doped carbon supports, enabling precise control over Pd loading and coordination, yielding mostly atomically dispersed Pd species stabilized by acetylacetonate ligands.[16–18] While this method previously demonstrated high ORR-2e$^-$ activity and selectivity for H_2O_2 generation, the catalysts suffered from poor (electro)chemical stability.[17,39] To overcome this, we maintained the Pd loading at 1 wt.% and extended the strategy to N-, S-, and N/S-doped HCS. The combination of optimized deposition and heteroatom-rich environments enables uniform Pd dispersion with negligible nanoparticle formation. Importantly, the synthetic protocol preserves both the hollow architecture and the chemical functionality of the support, providing a robust and tunable platform for stabilizing isolated Pd sites.

2.2. Structural and Chemical Characterization

The structural integrity and atomic dispersion of Pd on heteroatom-doped HCS were investigated employing a combination of advanced electron microscopy and spectroscopy techniques. High-angle annular dark-field (HAADF) STEM imaging (Figure 2; Figure S6, Supporting Information) revealed isolated

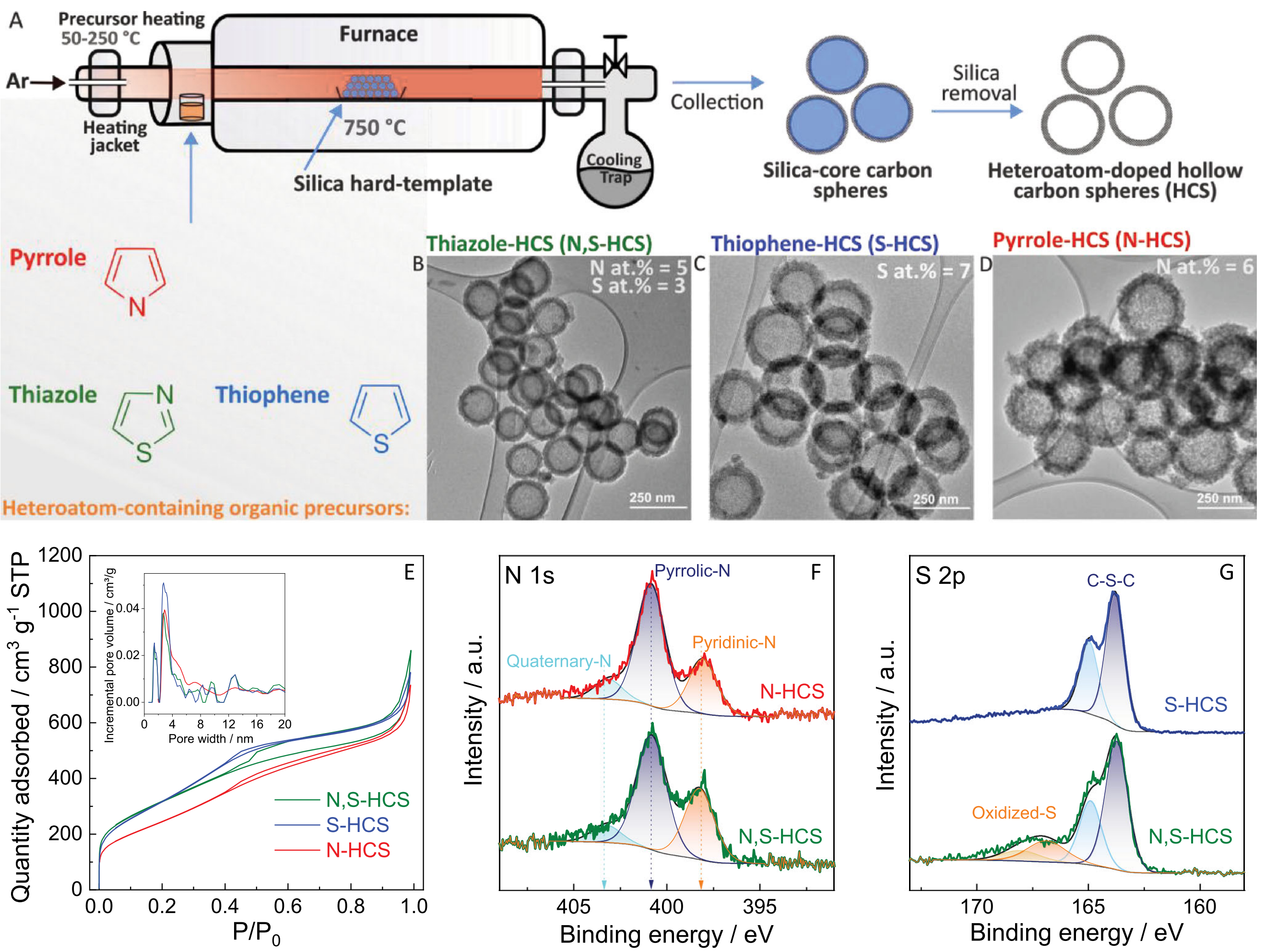

Figure 1. Synthesis and characterization of heteroatom-doped hollow carbon spheres (HCS) using chemical vapor deposition (CVD) of organic heterocycles. A) Molecular structures of the heteroatom-containing precursors used and the schematic illustration (created in Inkscape) of the CVD process using a silica template to obtain N-, S-, or N,S-doped HCS. B–D) TEM images of HCS derived from thiazole, thiophene, and pyrrole, showing uniform hollow structures. Elemental compositions (at.% by XPS) of N and S are indicated. E) N_2 adsorption–desorption isotherms and pore size distribution (inset) of the three HCS types, confirming mesoporosity. F) High-resolution (HR) XPS N 1s spectra of thiazole- and pyrrole-derived HCS. G) HR-XPS S 2p spectra of thiazole- and thiophene-derived HCS.

bright spots characteristic of atomically dispersed Pd species, with no evidence of extensive nanoparticle formation across all samples. Elemental mapping was used to confirm the homogeneous distribution of Pd, nitrogen, and sulfur within the carbon matrix. Notably, all Pd-containing samples retained well-defined spherical morphology, consistent with the templated structure of the HCS. Elemental distribution analysis via EDS mapping (Figure S7, Supporting Information) further confirmed uniform Pd dispersion in all samples. Complementary X-ray diffraction (XRD) analysis after Pd impregnation (cf. Figure 2G; Figure S2, Supporting Information) revealed negligible changes in the diffraction patterns to the bare HCS. All samples displayed the expected broad peaks characteristic of amorphous or turbostratic carbon, indicating no significant alteration in structural order. The absence of additional reflections suggests that no crystalline Pd particles or residual $Pd(acac)_2$ are present above the detection limit, consistent with the formation of atomically dispersed Pd species. Furthermore, cyclic voltammetry (Figure S8, Supporting Information) highlights the impact of Pd incorporation and heteroatom doping on the electrochemical behavior and double-layer capacitance of the hollow carbon supports. As expected for atomically dispersed Pd sites, no hydrogen underpotential deposition (H-UPD) peaks are observed in any of the Pd-containing samples, consistent with the absence of metallic Pd clusters.

2.3. Electronic State and Local Coordination of Pd Sites

To unravel the chemical environment and oxidation state of the atomically dispersed Pd species, we employed high-resolution X-ray photoelectron spectroscopy (XPS). The Pd 3d core-level spectra for all Pd/HCS samples (Figure 2H) exhibit well-defined doublets, with the Pd $3d_{5/2}$ peaks spanning from 336.4 to 338.2 eV and Pd $3d_{3/2}$ from 341.7 to 343.2 eV (Table S2, Supporting Information). These values are characteristic of Pd(II) species.[54–56] The absence of any signatures for metallic Pd, corroborated by

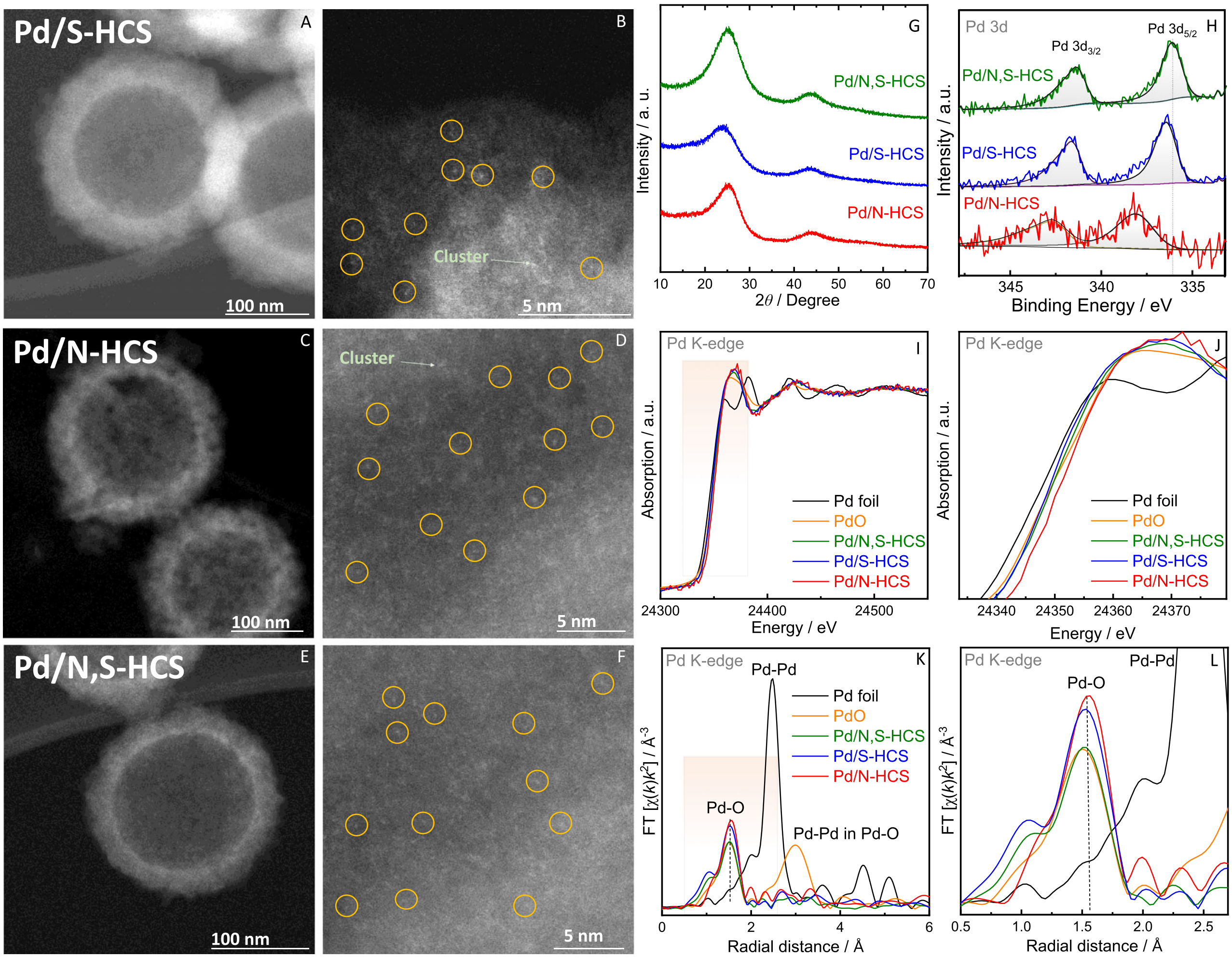

Figure 2. Structural and electronic characterization of Pd single-atom catalysts supported on heteroatom-doped HCS. A–F) Electron microscopy analysis of Pd/S-HCS (A–B), Pd/N-HCS (C,D), and Pd/N,S-HCS (E,F). High-resolution HAADF-STEM images (B,D,F) highlight atomically dispersed Pd atoms (yellow circles); occasional Pd clusters are also observed in (B,D). G) XRD patterns show broad peaks corresponding to amorphous carbon and the absence of Pd diffraction peaks, indicating high dispersion of Pd species. H) High-resolution Pd 3d XPS spectra of Pd/N-HCS, Pd/S-HCS, and Pd/N,S-HCS. I) Normalized Pd K-edge XANES spectra of the synthesized catalysts compared with Pd foil and PdO references. J) Enlarged view of the normalized Pd K-edge XANES spectra. K) Fourier-transformed k^3-weighted χ(k) EXAFS spectra of the same set of catalysts and references. L) Enlarged view of the normalized EXAFS spectra.

both XRD and TEM, reinforces the interpretation that Pd is atomically dispersed across all samples. Interestingly, some Pd/HCS samples exhibit a negative shift in binding energy compared to Pd/C SACs prepared using the same precursor (Pd(acac)$_2$), where the 3d$_{5/2}$ peak typically appears at ≈338.0 eV.[16,18,57] This shift suggests charge transfer from the support to the Pd centers, indicative of partial reduction and enhanced metal–support interaction. The most pronounced shift was observed for the co-doped Pd/N,S-HCS sample (336.4 eV), followed closely by Pd/S-HCS (336.5 eV). We attribute this effect to the synergistic electron redistribution within the carbon matrix, facilitated by thiophenic sulfur and nitrogen functionalities.[52,53,56] Sulfur, which possesses more valence electrons than carbon or nitrogen, can alter the local electronic environment by redistributing charge on the carbon surface.[26] This charge redistribution can enhance electron donation to the Pd sites, reinforcing the interaction between the metal center and the support. In contrast, Pd/N-HCS displayed higher binding energies (Pd 3d$_{5/2}$ at 338.2 eV), indicative of a more oxidized Pd environment. This can be explained by the nature of N species in the support: pyridinic-N, with its higher electron affinity, and pyrrolic-N, which tends to delocalize its lone pair into the π-system of the carbon framework, act as weaker electron donors.[58–61] As a result, Pd remains more oxidized in Pd/N-HCS, closer to the starting Pd(acac)$_2$ complex and previously reported Pd(acac)$_2$ impregnated on carbon materials, where the Pd organic complex interacts primarily with the support through van der Waals interactions and indirect electrostatic effects.[16–18,37]

To complement the XPS analysis and elucidate the local coordination environment of Pd, we conducted X-ray absorption spectroscopy (XAS), including both XANES and EXAFS measurements. The Pd K-edge XANES spectra of all Pd/HCS samples (Figure 2I) exhibit edge positions and white-line intensities that are significantly higher than those of metallic Pd, indicating that Pd is present in an oxidized state. This observation confirms that Pd does not exist in the metallic form but rather in a positively charged coordination environment. EXAFS analysis (Figure 2K) provides direct insight into the structural environment of Pd and confirms its atomic dispersion across all samples. The Fourier-transformed EXAFS spectra show no evidence of Pd–Pd scattering (at ≈2.5 Å, phase uncorrected), excluding the presence of metallic clusters. Instead, all synthesized samples display a prominent first-shell peak at ca. 1.5 Å (phase uncorrected), attributable to Pd—O coordination,[16,18] most likely originating from residual acetylacetonate derived from the precursor. Furthermore, comparison with PdO (c.f. Figure 2J) and $Pd(acac)_2$ references[16,62] confirms that the Pd—O coordination environment is largely preserved upon impregnation.[16,18] This coordination motif appears to persist regardless of the support's doping chemistry. Notably, the amplitude and width of the Pd—O peak vary among the doped samples. Pd/N-HCS exhibits the strongest and most well-defined peak, indicating a more uniform coordination environment and possibly higher coordination numbers. In contrast, Pd/N,S-HCS, followed by Pd/S-HCS, shows a broader and weaker Pd—O signal, consistent with reduced coordination number, likely induced by sulfur's steric and electronic influence.[26,53,56] To quantify these trends, we fitted the Pd K-edge EXAFS restricted to the first coordination shell in R-space using a Pd—O single-scattering model. The fits reproduce the spectra with low R-factors and give a first-shell distance of ≈2.00 Å for all supports. Coordination numbers are modestly below four, with the lowest value on the N, S-HCS (≈3.2), consistent with an under-coordinated Pd—O environment on this support (Table S3 and Figure S8, Supporting Information). It should be noted that we exclude Pd—N and Pd—C as first-shell assignments on EXAFS. Those shells would typically fit at longer distances (≈2.05 Å for Pd—N,[63] ≈2.15 Å for Pd—C,[64]), whereas our fits converge at ≈2.00 Å with low R-factors. In addition, previous literature[65] places the phase-uncorrected Pd—N first-shell FT peak near ≈1.45 Å (with Pd—O at ≈1.52 Å). In a direct comparison of undoped HCS and N-doped HCS, the phase-uncorrected first-shell peak of the N-doped sample appears at the same or slightly longer R than that of the undoped sample and aligns with $PdO/Pd(acac)_2$ references. The identical peak position across undoped and N-doped HCS indicates that the first shell does not depend on nitrogen functionalities, which is consistent with our synthesis route: Pd was introduced as $Pd(acac)_2$ under non-pyrolytic, low-temperature conditions (≤40 °C) without subsequent washing steps. Such conditions do not provide the driving force for the formation of covalent Pd—N or Pd—C bonds, favoring coordination to oxygenated surface functionalities. These observations are consistent with the XPS-derived trends and collectively suggest that heteroatom doping modulates Pd coordination indirectly by altering the local electronic and steric landscape of the carbon matrix. In Pd/N-HCS, $Pd(acac)_2$ is largely stabilized via van der Waals and electrostatic interactions, similar to its interaction in pristine carbon materials.[16–18,37] In contrast, in S-containing samples, additional stabilization arises from charge redistribution across the support surface. This effect is driven by the presence of heteroatoms with different atomic radii and electronegativities, which subtly influence the geometric configuration of the cationic Pd complex and modulate the energy levels of its d orbitals.[16–18,26] This nuanced interplay, combining van der Waals interactions, electrostatic effects, and soft donor–acceptor interactions, results in localized distortions in the Pd coordination sphere.

2.4. Electrocatalytic ORR Performance and H_2O_2 Selectivity

The electrocatalytic performance of the Pd-SACs supported on heteroatom-doped HCS was evaluated for the ORR in acidic media. As shown in **Figures 3** and S10 (Supporting Information), linear sweep voltammetry (LSV) measurements using an RRDE setup were conducted to compare both activity and selectivity across Pd/N-HCS, Pd/S-HCS, and Pd/N,S-HCS, using Pd/Vulcan as a benchmark.

Among all samples, Pd/N-HCS delivered the highest disk current density within the diffusion-controlled region, reaching −3.69 mA cm^{-2} at 0.2 V_{RHE}, surpassing Pd/Vulcan (−3.55 mA cm^{-2}). In comparison, Pd/S-HCS and Pd/N,S-HCS exhibited slightly lower current densities (−2.71 and −3.03 mA cm^{-2}). Regarding ORR onset potential, Pd/Vulcan and Pd/N-HCS showed the most positive values (≈0.75 and ≈0.70 V_{RHE}), followed by Pd/N,S-HCS and Pd/S-HCS (≈0.66 and ≈0.54 V_{RHE}), indicating that the electronic environment around Pd is highly sensitive to the nature and interaction with the support material.

In terms of selectivity, Pd/N-HCS exhibited a slightly reduced H_2O_2 selectivity (≈80%) across the 0.1–0.6 V_{RHE} potential range compared to Pd/S-HCS and Pd/N,S-HCS, both of which reached ≈90% (cf. Figure 3B). Pd/Vulcan, by contrast, achieved only ≈70% H_2O_2 selectivity in the same potential window. These differences can be attributed to variations in the electronic environment of Pd, modulated by the nature of the heteroatom-doped carbon supports. Specifically, sulfur doping, either alone or combined with nitrogen, was found to suppress overall ORR activity while simultaneously promoting H_2O_2 formation. XPS and XAS analyses indicate that S-doped and N,S-co-doped supports donate electron density to the atomically dispersed Pd centers. This redistribution of charge modifies the local electronic states of Pd, weakening the interaction with the *OOH intermediate by making electron transfer less favorable. The reduced *OOH binding energy suppresses the 4e^- reduction pathway to water and instead promotes the 2e^- ORR pathway, thereby enhancing H_2O_2 production.[29,34] In contrast, Pd sites on N-doped HCS and undoped Vulcan are more electron-deficient, leading to stronger O_2 adsorption and *OOH stabilization, which enhances the ORR kinetics at the expense of H_2O_2 selectivity.[34] Benchmarking against literature (Table S4, Supporting Information) confirms that our Pd/HCS and Pd/Vulcan catalysts deliver a competitive balance of activity and superior H_2O_2 selectivity compared to state-of-the-art Pd and Pt references. In the case of Pd/Vulcan, the limited presence of surface functional groups may result in weaker metal–support interactions. While this can lead to high initial activity, it compromises long-term structural integrity due to Pd leaching and insufficient anchoring, as previously observed.[39]

2.5. Stability Evaluation

In order to test the general stability of the catalysts, two H_2O_2-specific accelerated stress tests (ASTs) were conducted in acidic

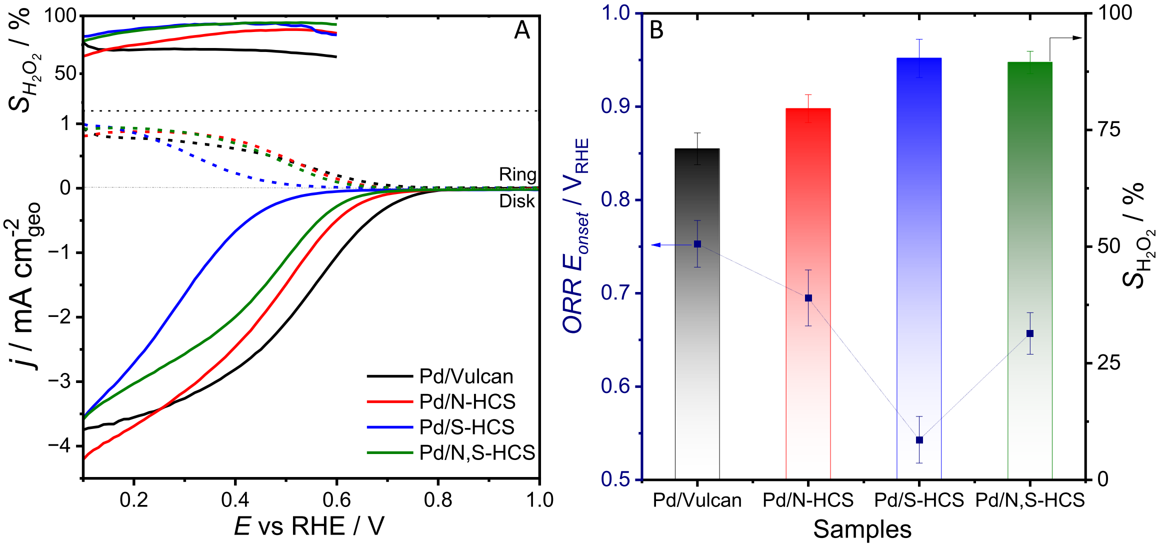

Figure 3. Electrocatalytic ORR activity and H_2O_2 selectivity of Pd single-atom catalysts. A) Linear sweep voltammetry (LSV) curves recorded using a rotating ring-disk electrode (RRDE) at 1600 rpm in O_2-saturated 0.1 M $HClO_4$ (scan rate: 10 mV s^{-1}, starting from 0.1 V_{RHE}). The corresponding H_2O_2 selectivity ($S_{H_2O_2}$) is shown as a function of potential (top panel), calculated from RRDE ring and disk currents. B) Summary of ORR onset potentials (defined at −0.1 mA cm^{-2}) and average H_2O_2 selectivity across the potential range of 0.1–0.6 V_{RHE} for all catalysts. Error bars denote 95% confidence intervals from independent measurements ($n \geq 3$).

media.[39] In AST 1, square-wave potential cycling between open circuit potential (OCP, 0.82 V_{RHE}) and a lower potential (LPL, set at 0.16 V_{RHE}, c.f. Table S5, Supporting Information) was applied to simulate degradation typically encountered during ORR. In contrast, AST 2 was used to evaluate the chemical effect of H_2O_2 exposure by subjecting the catalysts to prolonged contact with peroxide-rich environments in the absence of applied potential, thereby focusing on leaching or structural degradation mechanisms driven solely by H_2O_2.

As illustrated in **Figure** 4A–C, comparison of the beginning-of-life (BOL) and end-of-life (EOL) LSV curves shows that all Pd SACs supported on heteroatom-doped HCS exhibited significantly better electrochemical stability than Pd/Vulcan. After AST 1, Pd/Vulcan showed a marked degradation, with a negative shift in onset potential (≈0.12 V) and a current density loss of ≈1.2 mA cm^{-2} at 0.2 V_{RHE}. In contrast, Pd/N-HCS exhibited a smaller potential shift (≈0.07 V) and a more moderate current density loss (≈0.7 mA cm^{-2}). Notably, Pd/S-HCS and Pd/N,S-HCS demonstrated the most stable performance, with nearly unchanged onset potentials and minimal current losses (≈0.35 mA cm^{-2}, on average). These results suggest that sulfur incorporation, either alone or in conjunction with nitrogen, effectively stabilizes the Pd active sites under potential-driven degradation. This stability trend (Pd/S-HCS > Pd/N,S-HCS > Pd/N-HCS > Pd/Vulcan) aligns with increasing sulfur content and is consistent with literature reports linking electron-rich metal centers to improved resistance against oxidative corrosion.[26,66,67] These findings are supported by quantitative comparisons in Figure 4G,H. The relative current retention at 0.2 V_{RHE} (Figure 4G) reveals that both Pd/S-HCS and Pd/N,S-HCS retained over 85% of their initial activity after AST 1, while Pd/Vulcan dropped below 50%. Additionally, differential onset potential analysis (Figure 4H) shows that Pd/S-HCS and Pd/N,S-HCS maintained nearly unchanged onset potentials, whereas Pd/Vulcan experienced a substantial decline, further confirming their enhanced electrochemical resilience. Only minor variations were observed in the N_2-saturated cyclic voltammetric profiles after ASTs, both in terms of double-layer capacitance and the redox features associated with the quinone/hydroquinone couple, suggesting that the carbon supports remained largely unaltered.

In our previous work,[39] we observed that the decline in activity of Pd-SAC on Vulcan was due to the demetallation, where the relatively weak interaction between Pd and the carbon Vulcan, was attributed to the nature of the acetylacetonate ligand, which enhanced the susceptibility of Pd to leaching into the electrolyte driven by repetitive oxidation and reduction cycles on the catalyst surface.[68–72] XPS and XAS results support this mechanism, showing that sulfur doping enhances the electronic interaction between the Pd center and the support, partially reducing Pd and improving its stability. These effects are also reflected in the H_2O_2 selectivity data (Figure 4I). After AST 1, Pd/Vulcan's selectivity declined significantly (from ≈71% to 59%), while Pd/N-HCS showed a smaller reduction. Pd/S-HCS and Pd/N,S-HCS maintained high selectivity of ≈90%, with Pd/S-HCS even improving post-AST, suggesting that sulfur doping does not only stabilizes Pd but also preserves a favorable electronic structure for the $2e^-$ ORR pathway.

To isolate the chemical impact of peroxide exposure, we conducted AST 2 by immersing the catalysts in 10 mM H_2O_2-containing electrolyte solution without applied potential. As shown in Figure 4D–F, Pd/Vulcan displayed poor stability, with a ≈0.12 V negative shift in onset potential and a current density loss of ≈0.9 mA cm^{-2} at 0.2 V_{RHE}. Pd/N-HCS showed only minor changes (≈0.3 mA cm^{-2} loss), while Pd/S-HCS retained both onset potential and current density, highlighting its strong chemical stability. Remarkably, Pd/N,S-HCS combined the activity of Pd/N-HCS with the stability of Pd/S-HCS, maintaining a high current density and stable profile after H_2O_2 exposure.

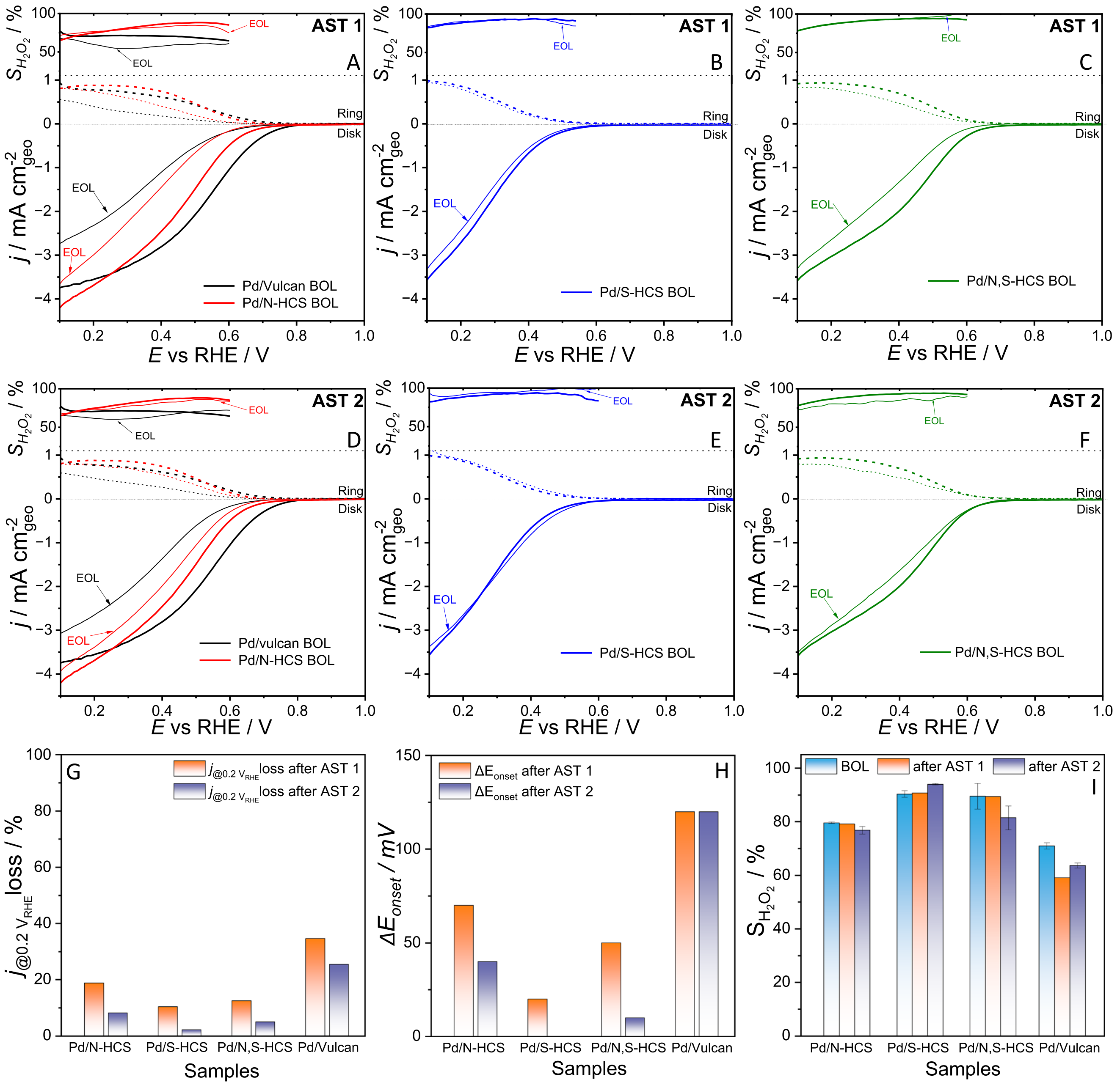

Figure 4. Electrocatalytic stability of Pd single-atom catalysts under accelerated stress testing (AST). Linear sweep voltammetry (LSV) curves for Pd/N-HCS, Pd/S-HCS, and Pd/N,S-HCS, compared to Pd/Vulcan. The curves were recorded before and after AST 1 A–C) and AST 2 D–F) using an RRDE at 1600 rpm in O_2-saturated 0.1 M $HClO_4$ (scan rate: 10 mV s^{-1}, starting from 0.1 V_{RHE}). The corresponding H_2O_2 selectivity ($S_{H_2O_2}$) is shown as a function of potential (top panel), calculated from RRDE ring and disk currents. G) Percentage loss of current density ($j_{@0.2V}$ loss): The $j_{@0.2V}$ loss = (($j_{@0.2V\ BOL}$ - $j_{@0.2V\ EOL}$) / $j_{@0.2V\ BOL}$) × 100. H) Differential ORR onset potential: The E_{onset} at −0.1 mA cm^{-2}, and the difference between EOL and BOL onset potentials. I) Values of selectivity toward H_2O_2 production before and after applying different ASTs. Error bars indicate mean ± SD from ≥2 independent runs per sample and AST. AST protocols are described in section "Accelerated Stress Test Protocols (AST 1 and AST 2).

Selectivity trends after AST 2, presented in Figure 4I, align with these findings. Pd/Vulcan showed a ≈7% drop in H_2O_2 selectivity (from ≈71% to ≈64%), while Pd/N-HCS and Pd/N,S-HCS exhibited smaller declines (from 79.6% to 76.8%, and 89.5% to 81.5%, respectively). Conversely, Pd/S-HCS demonstrated a surprising increase in selectivity (from 90% to 94%), reinforcing the idea that sulfur-rich environments do not only stabilize Pd but also suppress the 4e$^-$ ORR pathway. Together, the expanded analysis in Figure 4G–I provides quantitative support for the enhanced stability and selectivity retention of S- and N,S-doped catalysts. These results emphasize the critical role of heteroatom doping in achieving robust Pd–support interactions that resist both electrochemical and chemical degradation, ultimately enabling long-term H_2O_2 production.

To further elucidate the role of heteroatom doping and assess the influence of pore confinement on catalyst stability, we synthesized an undoped HCS using divinylbenzene (DVB) as the molecular precursor. The synthetic route mirrored that used for the heteroatom-doped HCS materials with slight modification,[73] resulting in relatively comparable morphology and textural properties (Table S6 and Figures S11 and S12, Supporting Information). Additionally, to isolate the specific contribution of sulfur doping, we prepared an S-doped Vulcan carbon (S content ≈1.1 at.%) via post-synthetic modification. Comprehensive characterization of both undoped-HCS and S-Vulcan before and after Pd impregnation is presented in Figures S11–S20 (Supporting Information). Consistent with previous results, X-ray absorption spectroscopy (XAS, Figure S19, Supporting Information) revealed trends similar to those observed for Pd/N-HCS and Pd/S-HCS. Both Pd/undoped-HCS and Pd/S-Vulcan displayed features indicative of both intact impregnation of $Pd(acac)_2$ when undoped HCS is used as the support and an observable local coordination distortion driven by sulfur doping, suggesting that S-induced structural modification of the Pd environment occurs independently of the underlying carbon support.

Figure S21 (Supporting Information) shows the RRDE polarization curves and corresponding H_2O_2 selectivity profiles for Pd/S-Vulcan and Pd/Undoped-HCS before and after exposure to AST 1 and AST 2. Consistent with the behavior observed for the S-doped HCS samples, Pd/S-Vulcan exhibited significantly enhanced stability under both electrochemical and chemical stress conditions compared to its undoped counterpart. After AST testing, the ORR onset potential displayed only a slight negative shift (≈30 mV after AST 1 and ≈10 mV after AST 2), while the current density at 0.2 V_{RHE} decreased only marginally (≈0.2 mA cm^{-2}). Importantly, the H_2O_2 selectivity remained consistently high, averaging ≈78%. These results reinforce the conclusion that S-doping, while slightly increasing ORR overpotential, markedly improves both stability and selectivity toward the $2e^-$ pathway by strengthening metal–support interactions under oxidative stress.

In contrast, Pd supported on undoped HCS exhibited a more pronounced performance degradation, characterized by an average negative shift of ≈85 mV in onset potential and a current density loss of ≈0.3 mA cm^{-2} at 0.2 V_{RHE} following AST 1 and 2 (c.f. Figure S21, Supporting Information). No significant changes in selectivity were observed. Nevertheless, its performance surpassed that of Pd supported on undoped Vulcan carbon, indicating that the hollow carbon sphere architecture contributes an additional stabilizing effect. We tentatively attribute this to pore confinement, which likely promotes the re-deposition of leached Pd species within the internal porous network, thereby partially mitigating irreversible metal loss.

2.6. Real-Time Pd Dissolution Monitoring Using Operando ICP-MS

To directly quantify Pd dissolution during operation, we employed real-time monitoring via operando channel flow electrochemical cell (CFC) measurements coupled to inductively coupled plasma mass spectrometry (ICP-MS), as schematically illustrated in Figure S22 (Supporting Information). The dissolution protocol involved two trapezoidal potential sweeps ranging from 0 to 1.0 V_{RHE} and 0 to 1.6 V_{RHE}, with a scan rate of 2 mV s^{-1} and 10-min holding periods at each plateau. These values were selected to probe both the ORR potential window and oxidative conditions known to promote carbon corrosion in acidic media.[74,75]

The operando ICP-MS results (**Figure 5**) reveal that Pd dissolution is strongly potential-dependent across all samples. Notably, Pd supported on undoped carbon materials (Pd/Vulcan and Pd/undoped-HCS) exhibited significantly higher dissolution rates. At 1.0 V_{RHE}, a potential relatively close to OCP, their dissolution was on average 2.1 times greater than that of Pd/S-Vulcan and ≈60 times higher than Pd supported on heteroatom-doped HCS (c.f. Figure 5C,D). Under these moderate electrochemical conditions, the cumulative Pd loss after 10 min at the applied potential was ≈10% for Pd/Vulcan, 6% for Pd/Undoped-HCS, 5% for Pd/S-Vulcan, 0.5% for Pd/N-HCS, 0.3% for Pd/S-HCS, and 0.2% for Pd/N,S-HCS These results underscore the stabilizing effect of sulfur and nitrogen doping under moderate electrochemical stress. To observe the influence of higher upper potential limits and the impact of carbon corrosion to the Pd-dissolution, the protocol was adapted to a UPL of 1.6 V_{RHE}. Here, a sharp increase in Pd dissolution was observed for all S-doped samples. For instance, Pd/S-Vulcan exhibited 2.3x more Pd dissolution than Pd/Vulcan, while Pd/S-HCS showed 1.6x more dissolution than Pd/undoped-HCS and ≈9x more than Pd/N-HCS (c.f. Figure 5; Figure S23, Supporting Information). This unexpected trend may be associated with reduced anchoring strength or structural stability of the S-doped carbon matrix under highly oxidizing conditions such as 1.6 V_{RHE}. At such potentials, sulfur atoms may be oxidized to higher oxidation states or leached as sulfur-containing moieties,[76–78] further weakening the support. In addition, the larger atomic radius of S can induce lattice strain and create defect sites, which, although catalytically beneficial at moderate potentials,[51,79] may compromise the structural integrity of the carbon network and reduce Pd anchoring strength under severe anodic polarization. In contrast, Pd/N-HCS demonstrated the lowest dissolution under these harsh oxidative conditions, suggesting that nitrogen doping improves the oxidative resilience of the carbon support. This result aligns with previous reports of enhanced corrosion resistance in nitrogen-doped carbon frameworks.[50,51,80] Importantly, the N,S-co-doped sample (Pd/N,S-HCS) consistently showed minimal Pd dissolution across both potential windows, ranking second-best under high potential stress. This performance indicates a potential synergistic contribution from both nitrogen and sulfur dopants: nitrogen may help maintain the structural integrity of the carbon matrix, while sulfur is likely to enhance metal–support interactions. These combined effects appear to mitigate Pd demetallation and contribute to the stabilization of cationic Pd species across a broad operational range. We note, however, that operando ICP-MS quantifies dissolution rather than site geometry; confirmation that Pd remains atomically dispersed after ASTs will require dedicated post-AST structural characterization (HAADF-STEM/XAS), which is underway and will be reported separately.

Taken together, these operando results demonstrate that rational heteroatom doping—particularly N,S co-doping—plays a critical role in stabilizing isolated Pd sites not only under ORR-relevant conditions but also in harsh oxidative environments. These insights emphasize the need to optimize both the electronic structure and structural stability of metal–support

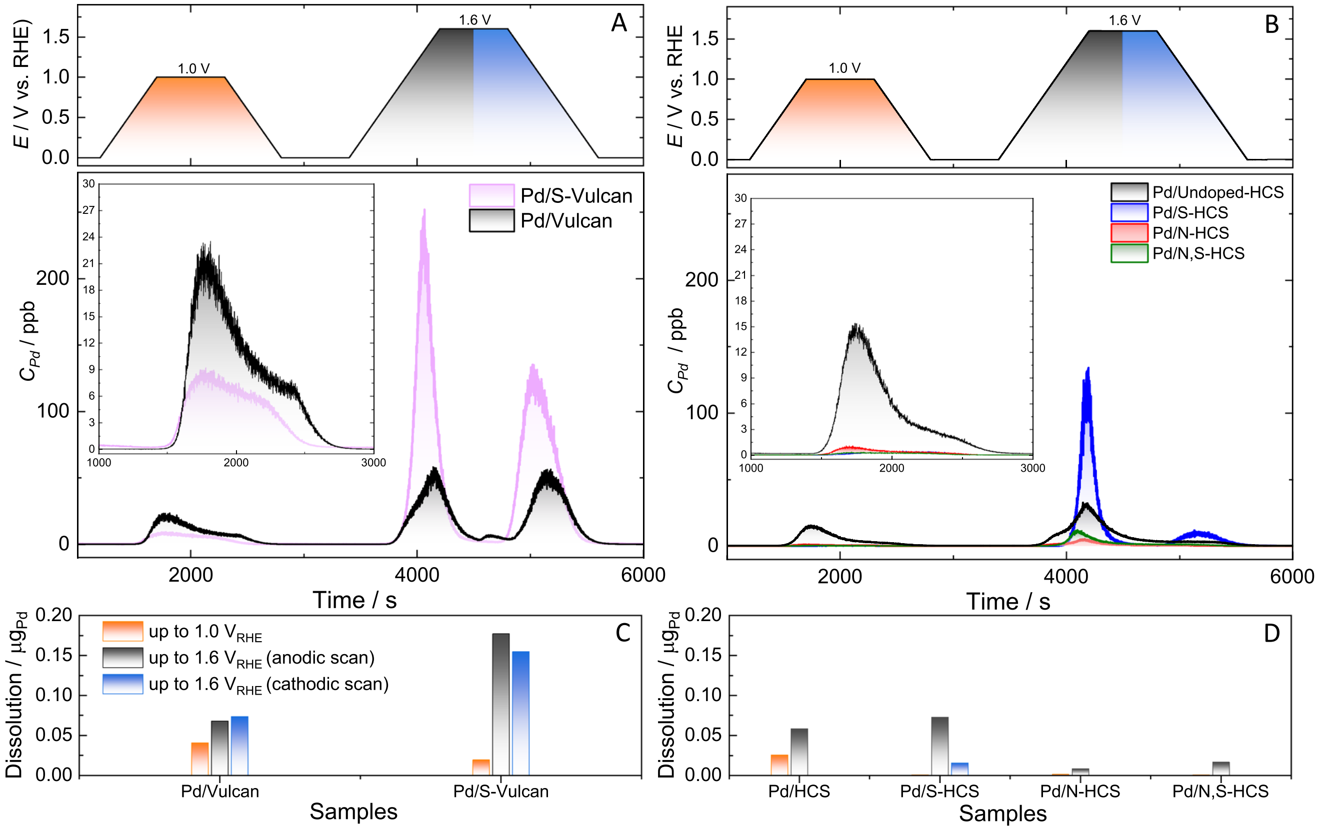

Figure 5. Operando Pd dissolution analysis of SACs in N_2-saturated 0.1 M $HClO_4$. A,B) Real-time Pd dissolution profiles recorded via ICP-MS during trapezoidal potential steps between 0 and 1.0 V_{RHE} and 0 and 1.6 V_{RHE} for Pd SACs supported on (A) Vulcan carbon and (B) heteroatom-doped HCS. C,D) Quantification of total Pd dissolved per potential step for each catalyst, highlighting the influence of support composition and doping on electrochemical stability.

interactions to mitigate catalyst degradation during operation. Given the tunable electron-donating and -withdrawing characteristics of nitrogen and sulfur species, N,S co-doping—to date most commonly realized via pyrolysis to stabilize single-atom Pt, Pd and 3d metals on carbon[21,31,81–84]—offers strong potential to tailor the coordination environment and improve the stability and selectivity of SACs for the 2e⁻ ORR and beyond. Further exploration of metal–organic complex approaches, with or without subsequent heat treatment to modulate metal–dopant interactions, should inform the design of next-generation single-atom electrocatalysts.

3. Conclusion

In summary, we have shown how heteroatom-functionalized carbon supports can be engineered to stabilize Pd single-atom catalysts under harsh electrochemical conditions. Operando ICP–MS and AST experiments revealed that sulfur doping enhances metal–support interactions and suppresses Pd dissolution at low potentials, while nitrogen doping maintains Pd site integrity even under highly oxidative conditions. Notably, N,S co-doped hollow carbon spheres exhibited minimal degradation and preserved atomic dispersion across a broad operational range. This unique performance arises from the cooperative electronic effects of the dopants, which reinforce Pd–support binding and mitigate demetallation. These results provide valuable insight into degradation mechanisms in ligand-containing SACs and highlight heteroatom co-doping as a promising strategy for designing stable, selective electrocatalysts for sustainable H_2O_2 production.

4. Experimental Section

Synthesis of Hollow Carbon Spheres (HCS): Hollow carbon spheres (HCS) were synthesized using a template-assisted approach, employing mesoporous silica as the sacrificial core (SiO_2@$mSiO_2$ hard template), as described elsewhere.[85] The deposition of the carbon shell and heteroatom doping were performed using a chemical vapor deposition (CVD) method at high temperatures under an inert atmosphere, following an adaptation of a previously reported procedure for mesoporous hollow graphitic spheres. A key modification was the omission of the graphitization step, which is typically catalyzed by iron. By replacing Ferrocene (iron precursor) by other heterocyclic compounds, the resulting HCS were obtained as precise replicas of the silica templates, avoiding the formation of highly graphitic domains. The carbon and dopant precursors were introduced by CVD at 750 °C with a heating rate of 10 K min^{-1} under argon (Ar, 99.999%, 100 mL min^{-1}). Different precursors were used to obtain heteroatom-functionalized HCS materials: Thiophene (C_4H_4S, ≥99%) served as both the carbon and sulfur precursor, thiazole (C_3H_3NS, ≥99%) introduced both N and S heteroatoms into the carbon framework, and pyrrole (C_4H_5N, ≥99%) introduced pyrrolic-N sites into the carbon structure. The SiO_2@$mSiO_2$ hard template was placed in a crucible at the center of a tube furnace, while the precursor was placed upstream in a separate chamber equipped with a heating jacket. Once the target temperature of 50 °C below the dwelling temperature (700 °C) was reached, the heating jacket was adjusted to 20 °C above the boiling point of the respective precursor, ensuring controlled evaporation. The precursor vapors were carried toward the silica template by the Ar flow, allowing uniform deposition. After 90 min, both the heating chamber and furnace were naturally cooled to room temperature (RT). The material was then carbonized at 850 °C for 4 h (10 K min^{-1}) under an Ar flow of 100 mL min^{-1}. The silica template was removed by selective etching in hydrofluoric acid (7 mL of 40 wt.% HF per gram of composite) at room temperature overnight, followed by thorough washing with deionized water and ethanol until neutral pH was reached. The resulting HCS materials (S-HCS, N-HCS, and N,S-HCS) were dried at 80 °C overnight.

For comparative studies, undoped HCS and S-doped Vulcan carbon were synthesized. Undoped HCS was synthesized using a similar hard-templating strategy with slight modifications. The same porous core–shell silica template and annealing conditions were used; however, carbon infiltration was performed using divinylbenzene (DVB), as described in detail elsewhere.[73] S-doped Vulcan carbon was prepared via post-treatment of Vulcan carbon (Cabot, Vulcan XC72R), which was first oxidized for 24 h in nitric acid (HNO_3) at 70 °C, then washed and dried. The oxidized Vulcan was then heat-treated with elemental sulfur in a tube furnace at 500 °C, followed by washing with toluene and drying under Schlenk vacuum at 100 °C.

Preparation of Pd SACs on HCS: Carbon-supported sub-nanocluster palladium catalysts were prepared via wet impregnation, using palladium(II) acetylacetonate (Pd(acac)_2, Aldrich, 99%) as the metal precursor, following a previously reported procedure.[17] The synthesis began by drying the selected carbon support at 80 °C under vacuum for at least 2 h in a Schlenk flask under magnetic stirring. After drying, 100 mg of the carbon support (S-HCS, N-HCS, N,S-HCS, HCS, Vulcan, or S-Vulcan) was transferred to a separate Schlenk flask. In parallel, 2.8 mg of Pd(acac)_2 was dissolved in 2.8 mL of extra-dry acetone (Aldrich, sealed under nitrogen). The resulting solution was slowly added dropwise to the carbon-containing Schlenk flask using a syringe pump at a controlled flow rate of 0.5 mL h^{-1} under continuous stirring. This procedure yielded a nominal Pd content of ≈1.0 wt.% (relative to carbon) based on precursor stoichiometry; no post-washing was applied. The mixture was stirred for 2 h at room temperature, followed by drying at 40 °C under nitrogen flow for 16 h.

Morphological and Structural Characterization: The morphology of the carbon samples (undoped and doped versions of HCS and Vulcan) was examined by transmission electron microscopy (TEM, JEOL JEM-2100F, 200 kV). The particle size distribution of Pd single atoms and atomic clusters supported on the carbon was determined by HAADF-STEM using a probe-corrected ThermoScientific Titan Themis 60–300 operated at 300 kV. The elemental composition and spatial distribution of N and S dopants, as well as Pd, C, and O elements, were analyzed using energy-dispersive X-ray spectroscopy (EDS) mapping.

The surface area and pore structure of the bare carbon materials were determined using nitrogen adsorption-desorption isotherms measured at 77 K on a Micromeritics ASAP 2020 system. The specific surface area was calculated using the Brunauer–Emmett–Teller (BET) method, while the pore size distribution was determined using the NLDFT method considering carbon slit pore geometry.

The chemical states of carbon, nitrogen, and sulfur were analyzed by X-ray photoelectron spectroscopy (XPS, Thermo Fisher K-Alpha+ system) equipped with a monochromatic Al Kα X-ray source. Deconvolution of the N 1s and S 2p regions was performed to distinguish different nitrogen (pyridinic-N, pyrrolic-N, graphitic-N) and sulfur (thiophenic-S, oxidized-S) species. The Pd-containing samples were analyzed using a SPECS instrument with a monochromatic Al K_α line at 1486.74 eV, 12.5 kV anode potential, and 24 mA beam current. The high-resolution spectrum for Pd 3d was measured with a pass energy of 20 eV, 0.1 s dwell time, and 0.05 eV steps. The C 1s signal of carbon was used for binding energy calibration and assigned to 284.7 eV. All XPS spectra were deconvoluted using CasaXPS peak fitting software with Shirley background subtractions. The Pd loading in the catalysts was confirmed by XPS.

X-ray absorption spectra at the Pd K-edge were collected at the BAM*line* at BESSY II in transmission mode.[86] The X-ray beam was monochromatized using a Si(111) double-crystal monochromator (DCM) with an energy resolution of $\Delta E/E = 2 \times 10^{-4}$. The beam size at the sample position was 5.0 mm (horizontal) × 1 mm (vertical). The measurements were performed in so-called continuous mode. This means the DCM is continuously moving and scanning a total of 1 keV range around the Pd K-edge (starting 100 eV below and ending 900 eV above) with ≈0.5 eV equidistant steps. The signal from the sample is extracted from the ratio between a first and a second ionization chamber (I0, I1), and a Pd reference foil is measured simultaneously with a third ionization chamber (I_2) (IC Spec from FBM-Oxford: https://www.fmb-oxford.com/products/detectors-diagnostics/ion-chambers/ic-spec/). The current produced by each ionization chamber is amplified by fast Keithley 428 current-to-voltage amplifiers. This amplified signal is, in turn, discretized by a frequency converter (V2F100 from quantum detectors: http://quantumdetectors.com/v2f100/) operable until 250 kHz. This frequency is read by a scaler unit function in the ZEBRA unit (Quantum detectors: https://quantumdetectors.com/products/zebra/). The ZEBRA unit collects synchronously the position of the angular encoder of the DCM (that corresponds to a given energy). Each full XAS spectrum was collected in 60 s. A total of 20 repetitions was merged to produce the final spectrum. Reference spectra of PdO were obtained from the NIMS Materials Data Repository (XAFS spectrum of Palladium(II) oxide - MDR), and Pd(acac)_2 data were retrieved from the open dataset reported in ref. [16] (available in the Research data repository (Cardiff University Research Portal)). Data alignment and normalization of the Pd K-edge XANES were performed using the conventional procedures implemented in Athena, and quantitative EXAFS analysis was carried out in Artemis/IFEFFIT. The Pd K-edge EXAFS of the samples was fitted in R-space over R = 1.15–2.00 Å. Fourier transforms were computed over k = 2.0–12.0 Å^{-1} with k-weightings of 1, 2, and 3. The fitted parameters were the coordination number (N), interatomic distance (R), disorder factor (σ^2) for the Pd—O path, and the photoelectron energy shift (ΔE_n). The amplitude reduction factor ($S_n{}^2$) was obtained from a Pd(acac)_2 reference (FEFF-based CN fixed at 4) and then held constant at 0.94 for all sample fits.

Thermogravimetric analysis (TGA) was performed using a Netzsch STA 449 F3 Jupiter thermal analysis instrument, coupled with a Netzsch QMS 403 D Aeolos mass spectrometer for evolved gas analysis. ≈5 mg of sample was used for each measurement. The temperature was ramped from 45 to 900 °C at a heating rate of 10 °C min^{-1}. Measurements were conducted under a controlled O_2 atmosphere with a flow rate of 40 mL min^{-1}.

Raman spectra were acquired using a WITec alpha 300 RA confocal Raman microscope (WITec, Germany) equipped with a 532 nm excitation laser operated at 0.2 mW. A Zeiss LD EC Epiplan–Neofluar 50×/0.55 objective lens was used for signal collection. Spectra were recorded with an integration time of 20 s and a single accumulation. The raw data were processed by applying a shape-based background subtraction (threshold = 1000) and smoothed using a moving mean filter (window size = 5). All spectra were normalized to the peak intensity at ≈1350 cm^{-1} to enable direct comparison of defect density across different samples.

Preparation of Working Electrode: The catalyst ink was prepared by dispersing 1.98 mg of catalyst powder in a solution containing 600 µL of ultrapure water and 400 µL of isopropanol. To enhance ink stability and adhesion, 8.6 µL of a 5 wt.% Nafion solution (Aldrich) was added, ensuring an ionomer-to-catalyst ratio of 0.2. The resulting mixture was subjected to horn sonication to achieve a uniform dispersion. Following sonication, 24 µL of the ink was carefully drop-cast onto a mirror-polished glassy carbon electrode and left to dry naturally at room temperature. The final palladium loading on the electrode surface was controlled at 2 µg cm^{-2}.

Electrochemical Measurements: Electrochemical experiments were conducted using a three-electrode setup in a glass electrochemical cell equipped with a fully automated setup containing dual potentiostats (Gamry, Interface 1010E), a rotating electrode system (PINE Research Instrumentation, WaveVortex), and a gas purging system integrated and controlled by Labview. All measurements were performed in 0.1 M $HClO_4$

electrolyte at 25 °C. The system employed a graphite rod as the counter electrode and a saturated Ag/AgCl reference electrode (Metrohm). The working electrode was a rotating ring-disk electrode (RRDE) assembly (PINE Research Instrumentation, AFE6R2GCPT), consisting of a 5.5 mm diameter glassy carbon disk (0.238 cm^2 geometric area) and a 2 mm thick platinum ring, embedded in a PEEK housing. Unless stated otherwise, all electrode potentials are reported versus the reversible hydrogen electrode (RHE) scale. The collection efficiency of the RRDE was experimentally determined to be 39.1%, using the $Fe(CN)_6]^{4-}/[Fe(CN)_6]^{3-}$ redox system under varying rotation speeds. Before conducting the ORR studies, the Pt ring of the RRDE electrode was cleaned electrochemically by cycling the potential between 0.1 and 1.4 V_{RHE} at 100 mV s^{-1} in an N_2-saturated electrolyte until stable cyclic voltammograms (CVs) were obtained. Background currents were recorded by performing CV scans in an N_2-saturated electrolyte over a potential range of 0.1–1.0 V_{RHE} at a 10 mV s^{-1} scan rate. Following O_2 saturation, ORR polarization curves were collected at a scan rate of 10 mV s^{-1} with the electrode rotating at 900 rpm. To facilitate the oxidation of generated H_2O_2, the Pt ring potential was maintained at 1.4 V_{RHE} throughout the ORR polarization measurements.

The H_2O_2 selectivity (S_{H2O2}) was determined based on the ring current (I_{ring}), disk current (I_{disk}), and the collection efficiency ($_{N}$) using the following equation:[87,88]

$$H_2O_2\ (\%) = 200\frac{I_{ring}}{N\left|I_{disk}\right| + I_{ring}} \tag{1}$$

Accelerated Stress Test Protocols (AST 1 and AST 2): The stability of the catalyst samples was evaluated using two H_2O_2-specific accelerated stress test (AST) protocols, adapted from previous literature.[23,39] AST 1 simulates the start-stop conditions of a proton exchange membrane (PEM) H_2O_2 fuel cell (H_2O_2-FC) or electrolyzer, applying a square wave voltammetry over 10 000 cycles between open circuit potential (OCP) and operational potential (OPP). These cyclic transitions induce oxidation-reduction processes, potentially leading to catalyst degradation and selectivity shifts. Performance was evaluated before (BOL) and after (EOL) cycling, with potentials set at 0.82 V_{RHE} (OCP) and 0.2 V_{RHE} (OPP).

AST 2 examines chemical stability under oxidative stress, mimicking prolonged exposure to H_2O_2. The catalyst-modified electrode was immersed in a 10 mᴍ H_2O_2 electrolyte for 12 h under continuous rotation (200 rpm) to evaluate degradation due to chemical attack. This corresponds to an equivalent H_2O_2 electrolysis operation of 12 h at 50 mA cm^{-2}, assuming a theoretical production rate of 0.6 ppm H_2O_2 h^{-1} mA^{-1} cm^{-2}. Electrochemical tests for all samples across the three ASTs were carried out with ≥2 independent replicates to ensure reproducibility and estimate variability.

ICP -MS Measurements: The in-house CFC was coupled with the ICP-MS (Nexion 2000B, Perkin Elmer) to monitor the dissolution of Pd in real time with a potentially resolved manner. Prior to each experiment, the ICP-MS was calibrated using a single-element Pd standard solution (Perkin Elmer), and its stability was validated throughout the measurements by continuously introducing an internal standard of ^{103}Rh (10 ppb in 0.1 ᴍ $HClO_4$, Perkin Elmer) during the measurements. Electrochemical dissolution measurements were performed using two consecutive trapezoidal potential scans ranging from 0 V_{RHE} to 1.0 V_{RHE}, then from 0 V_{RHE} to 1.6 V_{RHE}, each held at the upper potential limits for 10 min, with a scan rate of 2 mV s^{-1}. The two different upper potentials were chosen to elucidate the effect of support type and doping on mitigating the dissolution of Pd SACs. All electrodes were prepared with identical ink composition and film loading (200 µg cm^{-2}; same geometric area), and initial Pd content was comparable across catalysts (≈1.0 wt.%; see section "Preparation of Pd SACs on HCS"). The amount of dissolved Pd SACs was quantified by integrating the ICP-MS signals corresponding to each potential range, after subtracting the background signal, under a controlled electrolyte flow rate of 0.25 mL min^{-1}. All electrochemical measurements (for every sample) were performed at least two times in order to obtain statistically relevant data.

Supporting Information

Supporting Information is available from the Wiley Online Library or from the author.

Acknowledgements

The authors gratefully acknowledge the financial support provided by research funding agencies in Germany and Brazil. This work was funded by the Federal Ministry of Education and Research (BMBF, Germany) through the NanoMatFutur programme (SynKat, Grant No. 03XP0265), and in part by the Federal Ministry for Economic Affairs and Climate Protection (BMWK, Germany) under the POREForm project (Grant No. 03ETB027). H.W. and M.L. acknowledge the Initiative and Networking Fund of the Helmholtz Association for funding. P.B. thanks the Humboldt Foundation for funding. This study was also supported, in part, by the São Paulo Research Foundation (FAPESP, Brazil) under grant numbers 2019/04421-7, 2021/14194-8, 2021/12053-8, 2022/12895-1, and 2023/04230-2. Additional support was provided by the Brazilian National Council for Scientific and Technological Development (CNPq) under grants 465571/2014-0 and 303943/2021-1. XAS experiments were performed at the BAMline at the BESSY-II storage ring (Helmholtz Centre Berlin). The authors thank the Helmholtz-Zentrum Berlin für Materialien und Energie for the allocation of synchrotron radiation beamtime. The authors would like to thank Claudia Weidenthaler and Sebastian Leiting for the XPS measurements, and Thomas Böhm and Carina Götz for the Raman measurements.

Open access funding enabled and organized by Projekt DEAL.

Conflict of Interest

The authors declare no conflict of interest.

Data Availability Statement

The data that support the findings of this study are available from the corresponding author upon reasonable request.

Keywords

catalyst stability, demetallation, hetero-atom doping, hydrogen peroxide electrosynthesis, oxygen reduction reaction, single-atom catalysts

Received: June 29, 2025
Revised: August 29, 2025

---

[1] X. F. Yang, A. Wang, B. Qiao, J. Li, J. Liu, T. Zhang, *Acc. Chem. Res.* **2013**, *46*, 1740.
[2] M. B. Gawande, P. Fornasiero, R. Zbořil, *ACS Catal.* **2020**, *10*, 2231.
[3] F. Yang, H. Han, H. Duan, F. Fan, S. Chen, B. Yu Xia, Y.-L. He, *Adv. Energy Mater.* **2025**, *15*, 2405726.
[4] C. Zhu, S. Fu, Q. Shi, D. Du, Y. Lin, *Angew. Chem., Int. Ed.* **2017**, *56*, 13944.
[5] Y. Huang, J. Xiong, Z. Zou, Z. Chen, *Adv. Mater.* **2025**, *37*, 2312182.
[6] A. Kumar, G. Yasin, S. Ajmal, S. Ali, M. A. Mushtaq, M. M. Makhlouf, T. A. Nguyen, P. Bocchetta, R. K. Gupta, S. Ibraheem, *Int. J. Hydrogen Energy* **2022**, *47*, 17621.
[7] R. M. Reis, R. B. Valim, R. S. Rocha, A. S. Lima, P. S. Castro, M. Bertotti, M. R. V. Lanza, *Electrochim. Acta* **2014**, *139*, 1.

[8] H. Tang, H. Yin, J. Wang, N. Yang, D. Wang, Z. Tang, *Angew. Chem., Int. Ed.* **2013**, *52*, 5585.
[9] J. Meng, H. Lei, X. Li, J. Qi, W. Zhang, R. Cao, *ACS Catal.* **2019**, *9*, 4551.
[10] Y.-M. Zhao, G.-Q. Yu, F.-F. Wang, P.-J. Wei, J.-G. Liu, *Chem. – Eur. J.* **2019**, *25*, 3726.
[11] F.-F. Wang, Y.-M. Zhao, P.-J. Wei, Q.-L. Zhang, J.-G. Liu, *Chem. Commun.* **2017**, *53*, 1514.
[12] M. Mahyari, S. E. Hooshmand, H. Sepahvand, J. N. Gavgani, S. G. Hosseini, *Appl. Organomet. Chem.* **2020**, *34*, 5540.
[13] R. Venegas, K. Muñoz-Becerra, S. Juillard, L. Zhang, R. Oñate, I. Ponce, V. Vivier, F. J. Recio, C. M. Sánchez-Sánchez, *Electrochim. Acta* **2022**, *434*, 141304.
[14] Y. Wang, M. Wang, Z. Zhang, Q. Wang, Z. Jiang, M. Lucero, X. Zhang, X. Li, M. Gu, Z. Feng, Y. Liang, *ACS Catal.* **2019**, *9*, 6252.
[15] G. Zhang, Y. Jia, C. Zhang, X. Xiong, K. Sun, R. Chen, W. Chen, Y. Kuang, L. Zheng, H. Tang, W. Liu, J. Liu, X. Sun, W.-F. Lin, H. Dai, *Energy Environ. Sci.* **2019**, *12*, 1317.
[16] X. Sun, S. R. Dawson, T. E. Parmentier, G. Malta, T. E. Davies, Q. He, L. Lu, D. J. Morgan, N. Carthey, P. Johnston, S. A. Kondrat, S. J. Freakley, C. J. Kiely, G. J. Hutchings, *Nat. Chem.* **2020**, *12*, 560.
[17] J. S. Choi, S. Yoo, E. S. Koh, R. Aymerich-Armengol, C. Scheu, G. V. Fortunato, M. R. V. Lanza, Y. J. Hwang, M. Ledendecker, *Adv. Mater. Interfaces* **2023**, *10*, 2300647.
[18] Y. Yao, X. Zhang, Y. Cao, L. Liu, Y. Zhang, S. Zhang, *J. Am. Chem. Soc.* **2024**, *146*, 31053.
[19] X. Zhang, X. Xu, S. Yao, C. Hao, C. Pan, X. Xiang, Z. Q. Tian, P. K. Shen, Z. Shao, S. P. Jiang, *Small* **2022**, *18*, 2105329.
[20] J. Guo, J. Huo, Y. Liu, W. Wu, Y. Wang, M. Wu, H. Liu, G. Wang, *Small Methods* **2019**, *3*, 1900159.
[21] H. Shen, E. Gracia-Espino, J. Ma, K. Zang, J. Luo, L. Wang, S. Gao, X. Mamat, G. Hu, T. Wagberg, S. Guo, *Angew. Chem., Int. Ed.* **2017**, *56*, 13800.
[22] G. Bae, S. Han, H.-S. Oh, C. H. Choi, *Angew. Chem., Int. Ed.* **2023**, *62*, 202219227.
[23] J. S. Choi, G. V. Fortunato, D. C. Jung, J. C. Lourenco, M. R. V. Lanza, M. Ledendecker, *Nanoscale Horiz.* **2024**, *9*, 1250.
[24] K. Kumar, L. Dubau, M. Mermoux, J. Li, A. Zitolo, J. Nelayah, F. Jaouen, F. Maillard, *Angew. Chem., Int. Ed.* **2020**, *59*, 3235.
[25] P. Hu, Q. Zhang, X. Lu, Z. Zuo, *Catal. Sci. Technol.* **2024**, *14*, 2630.
[26] T. Zheng, X. Han, J. Wang, Z. Xia, *Nanoscale* **2022**, *14*, 16286.
[27] J. Xi, S. Yang, L. Silvioli, S. Cao, P. Liu, Q. Chen, Y. Zhao, H. Sun, J. N. Hansen, J.-P. B. Haraldsted, J. Kibsgaard, J. Rossmeisl, S. Bals, S. Wang, I. Chorkendorff, *J. Catal.* **2021**, *393*, 313.
[28] X. H. Xie, C. He, B. Y. Li, Y. H. He, D. A. Cullen, E. C. Wegener, A. J. Kropf, U. Martinez, Y. W. Cheng, M. H. Engelhard, M. E. Bowden, M. Song, T. Lemmon, X. S. Li, Z. M. Nie, J. Liu, D. J. Myers, P. Zelenay, G. F. Wang, G. Wu, V. Ramani, Y. Y. Shao, *Nat. Catal.* **2020**, *3*, 1044.
[29] C. H. Choi, M. Kim, H. C. Kwon, S. J. Cho, S. Yun, H. T. Kim, K. J. Mayrhofer, H. Kim, M. Choi, *Nat. Commun.* **2016**, *7*, 10922.
[30] H. C. Kwon, M. Kim, J.-P. Grote, S. J. Cho, M. W. Chung, H. Kim, D. H. Won, A. R. Zeradjanin, K. J. J. Mayrhofer, M. Choi, H. Kim, C. H. Choi, *J. Am. Chem. Soc.* **2018**, *140*, 16198.
[31] Q. Li, W. Chen, H. Xiao, Y. Gong, Z. Li, L. Zheng, X. Zheng, W. Yan, W.-C. Cheong, R. Shen, N. Fu, L. Gu, Z. Zhuang, C. Chen, D. Wang, Q. Peng, J. Li, Y. Li, *Adv. Mater.* **2018**, *30*, 1800588.
[32] F. D. Speck, M. T. Y. Paul, F. Ruiz-Zepeda, M. Gatalo, H. Kim, H. C. Kwon, K. J. J. Mayrhofer, M. Choi, C. H. Choi, N. Hodnik, S. Cherevko, *J. Am. Chem. Soc.* **2020**, *142*, 15496.
[33] Y. Mun, S. Lee, K. Kim, S. Kim, S. Lee, J. W. Han, J. Lee, *J. Am. Chem. Soc.* **2019**, *141*, 6254.
[34] J. Zhao, C. Fu, K. Ye, Z. Liang, F. Jiang, S. Shen, X. Zhao, L. Ma, Z. Shadike, X. Wang, J. Zhang, K. Jiang, *Nat. Commun.* **2022**, *13*, 685.
[35] S. Unsal, R. Girod, C. Appel, D. Karpov, M. Mermoux, F. Maillard, V. A. Saveleva, V. Tileli, T. J. Schmidt, J. Herranz, *J. Am. Chem. Soc.* **2023**, *145*, 7845.
[36] Z. Jiang, W. Sun, H. Shang, W. Chen, T. Sun, H. Li, J. Dong, J. Zhou, Z. Li, Y. Wang, R. Cao, R. Sarangi, Z. Yang, D. Wang, J. Zhang, Y. Li, *Energy Environ. Sci.* **2019**, *12*, 3508.
[37] S. Grimme, *Angew. Chem., Int. Ed.* **2008**, *47*, 3430.
[38] T. Lu, Q. Chen, *J. Comput. Chem.* **2022**, *43*, 539.
[39] G. V. Fortunato, D. C. Jung, J. C. Lourenço, P. Bhuyan, J. S. Choi, X. You, S. Lim, M. Melchionna, H. Sezen, J. P. Hofmann, P. Fornasiero, M. R. V. Lanza, M. Ledendecker, *ACS Catal.* **2025**, *15*, 8811.
[40] H. Hu, J. Wang, P. Tao, C. Song, W. Shang, T. Deng, J. Wu, *J. Mater. Chem. A* **2022**, *10*, 5835.
[41] Y. Cui, C. Ren, M. Wu, Y. Chen, Q. Li, C. Ling, J. Wang, *J. Am. Chem. Soc.* **2024**, *146*, 29169.
[42] K. Rigby, J.-H. Kim, *Curr. Opin. Chem. Eng.* **2023**, *40*, 100921.
[43] W. Li, Z. Guo, J. Yang, Y. Li, X. Sun, H. He, S. Li, J. Zhang, *Electrochem. Energy Rev.* **2022**, *5*, 9.
[44] Z. Lang, X. Wang, S. Jabeen, Y. Cheng, N. Liu, Z. Liu, T. Gan, Z. Zhuang, H. Li, D. Wang, *Adv. Mater.* **2025**, *37*, 2418942.
[45] J. Knossalla, J. Mielby, D. Göhl, F. R. Wang, D. Jalalpoor, A. Hopf, K. J. J. Mayrhofer, M. Ledendecker, F. Schüth, *ACS Appl. Energy Mater.* **2021**, *4*, 5840.
[46] M. D. Hossain, Q. Zhang, T. Cheng, W. A. Goddard, Z. Luo, *Carbon* **2021**, *183*, 940.
[47] T. Panja, D. Bhattacharjya, J.-S. Yu, *J. Mater. Chem. A* **2015**, *3*, 18001.
[48] Z. Qiang, Y. Xia, X. Xia, B. D. Vogt, *Chem. Mater.* **2017**, *29*, 10178.
[49] Y. Gao, Q. Wang, G. Ji, A. Li, J. Niu, *RSC Adv.* **2021**, *11*, 5361.
[50] G. V. Fortunato, M. S. Kronka, E. S. F. Cardoso, A. J. dos Santos, A. J. r. Roveda, F. H. B. Lima, M. Ledendecker, G. Maia, M. R. V. Lanza, *J. Catal.* **2022**, *413*, 1034.
[51] V. Perazzolo, E. Grądzka, C. Durante, R. Pilot, N. Vicentini, G. A. Rizzi, G. Granozzi, A. Gennaro, *Electrochim. Acta* **2016**, *197*, 251.
[52] D. Littlejohn, S.-G. Chang, *J. Electron Spectrosc. Relat. Phenom.* **1995**, *71*, 47.
[53] R. Sun, M. Zhu, J. Chen, L. Yan, L. Bai, J. Ning, Y. Zhong, Y. Hu, *ACS Nano* **2025**, *19*, 13414.
[54] M. C. Militello, S. J. Simko, *Surf. Sci. Spectra* **1994**, *3*, 395.
[55] M. Ledendecker, E. Pizzutilo, G. Malta, G. V. Fortunato, K. J. J. Mayrhofer, G. J. Hutchings, S. J. Freakley, *ACS Catal.* **2020**, *10*, 5928.
[56] L. Wang, M.-X. Chen, Q.-Q. Yan, S.-L. Xu, S.-Q. Chu, P. Chen, Y. Lin, H.-W. Liang, *Sci. Adv.* **2019**, *5*, aax6322.
[57] J. S. Choi, G. V. Fortunato, M. Malinovic, E. S. Koh, R. Aymerich-Armengol, C. Scheu, H. Wang, A. Hutzler, J. P. Hofmann, M. R. V. Lanza, M. Ledendecker, *Nano Energy* **2025**, *137*, 110811.
[58] R. Arrigo, M. E. Schuster, Z. Xie, Y. Yi, G. Wowsnick, L. L. Sun, K. E. Hermann, M. Friedrich, P. Kast, M. Hävecker, A. Knop-Gericke, R. Schlögl, *ACS Catal.* **2015**, *5*, 2740.
[59] Y.-X. Xiao, J. Ying, J.-B. Chen, Y. Dong, X. Yang, G. Tian, J. Wu, C. Janiak, K. I. Ozoemena, X.-Y. Yang, *Chem. Mater.* **2022**, *34*, 3705.
[60] L. Jia, D. A. Bulushev, O. Y. Podyacheva, A. I. Boronin, L. S. Kibis, E. Y. Gerasimov, S. Beloshapkin, I. A. Seryak, Z. R. Ismagilov, J. R. H. Ross, *J. Catal.* **2013**, *307*, 94.
[61] Y.-H. Li, T.-H. Hung, C.-W. Chen, *Carbon* **2009**, *47*, 850.
[62] E. Lesage-Rosenberg, G. Vlaic, H. Dexpert, P. Lagarde, E. Freund, *Appl. Catal.* **1986**, *22*, 211.
[63] N. Le Bris, J. Pineau, L. M. P. Lima, R. Tripier, *Coord. Chem. Rev.* **2022**, *455*, 214343.
[64] J. W. Sobczak, E. Sobczak, B. Lesiak, W. Palczewska, A. Kosinski, *J. Alloys Compd.* **1999**, *286*, 98.
[65] D. Huang, K. Rigby, W. Chen, X. Wu, J. Niu, E. Stavitski, J.-H. Kim, *Proc. Natl. Acad. Sci. USA* **2023**, *120*, 2216879120.
[66] E. F. Holby, G. F. Wang, P. Zelenay, *ACS Catal.* **2020**, *10*, 14527.
[67] G. Di Liberto, L. Giordano, G. Pacchioni, *ACS Catal.* **2023**, *14*, 45.

[68] E. Pizzutilo, S. J. Freakley, S. Geiger, C. Baldizzone, A. Mingers, G. J. Hutchings, K. J. J. Mayrhofer, S. Cherevko, *Catal. Sci. Technol.* **2017**, *7*, 1848.
[69] J. C. Meier, C. Galeano, I. Katsounaros, A. A. Topalov, A. Kostka, F. Schüth, K. J. J. Mayrhofer, *ACS Catal.* **2012**, *2*, 832.
[70] T. Imhof, R. K. F. Della Bella, B. M. Stuhmeier, H. A. Gasteiger, M. Ledendecker, *Phys. Chem. Chem. Phys.* **2023**, *25*, 20533.
[71] E. Pizzutilo, S. J. Freakley, S. Cherevko, S. Venkatesan, G. J. Hutchings, C. H. Liebscher, G. Dehm, K. J. J. Mayrhofer, *ACS Catal.* **2017**, *7*, 5699.
[72] A. A. Topalov, S. Cherevko, A. R. Zeradjanin, J. C. Meier, I. Katsounaros, K. J. J. Mayrhofer, *Chem. Sci.* **2014**, *5*, 631.
[73] J. Knossalla, D. Jalalpoor, F. Schüth, *Chem. Mater.* **2017**, *29*, 7062.
[74] S. J. Ashton, M. Arenz, *J. Power Sources* **2012**, *217*, 392.
[75] L. Castanheira, W. O. Silva, F. H. B. Lima, A. Crisci, L. Dubau, F. Maillard, *ACS Catal.* **2015**, *5*, 2184.
[76] X. Zhao, Q. Zhang, C.-M. Chen, B. Zhang, S. Reiche, A. Wang, T. Zhang, R. Schlögl, D. Sheng Su, *Nano Energy* **2012**, *1*, 624.
[77] J. Mitzel, Q. Zhang, P. Gazdzicki, K. A. Friedrich, *J. Power Sources* **2021**, *488*, 229375.
[78] J. Fu, M. Hou, C. Du, Z. Shao, B. Yi, *J. Power Sources* **2009**, *187*, 32.
[79] E. S. F. Cardoso, G. V. Fortunato, C. D. Rodrigues, M. R. V. Lanza, G. Maia, *Nanomaterials* **2023**, *13*, 2831.
[80] Y. Li, J. Li, Y.-G. Wang, X. Chen, M. Liu, Z. Zheng, X. Peng, *Int. J. Hydrogen Energy* **2021**, *46*, 13273.
[81] X. Li, W. Xu, L. Q. Le, S. Chen, L. Song, T. S. Choksi, X. Wang, *Chem Catalysis* **2023**, *3*, 100724.
[82] P. Zhu, W.-X. Shi, Y. Wang, Z.-M. Zhang, L. Li, C. An, *Nano Res.* **2023**, *16*, 6593.
[83] D. Wei, L. Chen, H. Zhao, L. Tian, S. Ramakrishna, D. Ji, *ACS Appl. Nano Mater.* **2023**, *6*, 11061.
[84] J. Zhang, Y. Zhao, C. Chen, Y.-C. Huang, C.-L. Dong, C.-J. Chen, R.-S. Liu, C. Wang, K. Yan, Y. Li, G. Wang, *J. Am. Chem. Soc.* **2019**, *141*, 20118.
[85] J. Knossalla, J. Mielby, D. Goehl, F. R. Wang, D. Jalalpoor, A. Hoepf, K. J. J. Mayrhofer, M. Ledendecker, F. Schueth, *ACS Appl. Energy Mater.* **2021**, *4*, 5840.
[86] A. Guilherme Buzanich, M. Radtke, K. V. Yusenko, T. M. Stawski, A. Kulow, C. T. Cakir, B. Röder, C. Naese, R. Britzke, M. Sintschuk, F. Emmerling, *J. Chem. Phys.* **2023**, *158*, 244202.
[87] U. A. Paulus, T. J. Schmidt, H. A. Gasteiger, R. J. Behm, *J. Electroanal. Chem.* **2001**, *495*, 134.
[88] O. Antoine, R. Durand, *J. Appl. Electrochem.* **2000**, *30*, 839.